

¹R. E. Nahory, Phys. Rev. 178, 1293 (1969).

²These processes have been discussed by H. J. Stocker and H. Kaplan, Phys. Rev. 150, 619 (1966); and experimental work prior to mid-1966 was summarized by H. J. Stocker, H. Levinstein, and C. R. Stannard, *ibid.* 150, 613 (1966).

³Q. H. F. Vrethen, J. Phys. Chem. Solids 29, 129 (1968).

⁴A. K. Walton and U. K. Mishra, J. Phys. C 1, 533 (1968).

⁵A. Mooradian and G. B. Wright, Solid State Commun. 4, 431 (1966).

⁶M. Cardona, Phys. Rev. 121, 752 (1961).

⁷H. Ehrenreich, Phys. Rev. 120, 1951 (1960).

⁸C. G. Olson and D. W. Lynch, Phys. Rev. 177, 1231 (1969).

⁹Similar effects in *p*-type InSb were studied in Ref. 2.

¹⁰J. Shah, R. C. C. Leite, and R. E. Nahory, Phys. Rev. 184, 811 (1969).

¹¹E. O. Kane, J. Phys. Chem. Solids 1, 249 (1957).

¹²K. Kreher, Fortschr. Physik 12, 489 (1964).

¹³R. L. Bowers and G. D. Mahan, Phys. Rev. 185, 1073 (1969).

¹⁴M. Reine, R. L. Aggarwal, B. Lax, and C. M. Wolfe, Phys. Rev. B 2, 458 (1970).

Electron Transport in InSb, InAs, and InP

D. L. Rode

Bell Telephone Laboratories, Murray Hill, New Jersey 07974

(Received 15 December 1970)

The calculation of electron-transport properties of direct-gap semiconductors has been generalized to include arbitrary electron degeneracy as well as scattering by ionized impurities and heavy holes. Conduction-band nonparabolicity and electron wave-function admixture are retained throughout the calculation of drift mobility and thermoelectric power. Extensive comparison of the results with experiment confirms the present description over wide ranges of temperature and ionized-impurity concentration. Effects of multivalley conduction due to electron transfer into L_{1c} satellite valleys appear in InSb above 700 °K (just below the melting point at ~ 780 °K) and in InP above 800 °K. The lowest satellite valleys of InAs are sufficiently remote from the conduction-band edge at Γ_{1c} that the results are expected to be accurate up to the melting point at ~ 1200 °K.

I. INTRODUCTION

Transport properties of electrons in direct-gap semiconductors can be conveniently derived by direct solution of the Boltzmann equation. Previous applications^{1,2} of this technique were directed toward calculations of drift mobility in ideally pure semiconductors. There is also considerable interest in accurate descriptions of impure crystals, from both the experimental and the theoretical points of view. In the former case, for example, one may take advantage of the sensitivity of mobility to ionized impurities in analyses of impurity content.³ In the latter case, highly doped materials allow one to probe regions of the conduction band in the neighborhood of the Fermi level, well above the band edge. Obviously, accurate calculations in conjunction with experimental data are helpful in exposing weaknesses of the theoretical model, particularly with regard to electron scattering by ionized impurities at low temperatures.⁴

The purpose of the present paper is to calculate electron-drift mobility and thermoelectric power for various temperatures and ionized-impurity concentrations. The formulation itself applies only to

conduction in the single Γ_{1c} minimum of direct-gap semiconductors; detailed comparison of the results with experiment helps to indicate the onset of multivalley conduction. Only in the extremes of high temperature or high free-electron concentration do multivalley effects become evident. For the remaining broad range of temperature and impurity concentration, the formulation presented in Sec. II will be seen to agree well with experiment in a *quantitative* as well as qualitative fashion.

In order to allow for wide ranges of temperature and electron concentration, it is necessary to generalize the earlier treatment¹ to include electron degeneracy and scattering by ionized impurities and holes. The appropriate formulation of the Boltzmann equation for Fermi-Dirac statistics is developed in Sec. II. Perturbation from equilibrium by a small electric field or temperature gradient leads to a linear-difference equation for the perturbed part of the distribution function.^{5,6} The effects of electron scattering are *formally* included in the difference equation. In Sec. III, the following scattering processes are evaluated explicitly: (i) piezoelectric scattering^{7,8} by transverse and longitudinal acoustic modes, (ii) deformation-potential

scattering⁹ by longitudinal acoustic modes, (iii) polar scattering^{10,11} by optical modes, (iv) heavy-hole scattering,⁶ and (v) ionized-impurity scattering.^{12,13} Material parameters suitable for calculations of mobility and thermoelectric power with no adjustable parameters are discussed in Sec. IV along with comparisons of theoretical and experimental results.

II. BOLTZMANN EQUATION WITH FERMI STATISTICS

The total probability distribution function for the electrons is $f_T(\vec{k}')$, where $\hbar\vec{k}$ is the crystal momentum. In the presence of an external electric field \vec{F} , f_T satisfies the Boltzmann equation for Fermi-Dirac statistics,¹⁴

$$(e/\hbar)\vec{F}\cdot\nabla_{\vec{k}}f_T = \int [s'f'_T(1-f_T) - sf_T(1-f'_T)] d\vec{k}'. \quad (1)$$

In Eq. (1), $f_T = f_T(\vec{k})$, $f'_T = f_T(\vec{k}')$, and the differential-scattering rates are $s = s(\vec{k}, \vec{k}')$ and $s' = s(\vec{k}', \vec{k})$. The integrals in Eq. (1) involving s and s' , respectively, yield probability fluxes for scattering *out from* and *into* the differential volume element $d\vec{k}$. In the measurement of low-field drift mobility the electric field is made vanishingly small. In this limit, the total distribution function can be written exactly as the sum of two parts. The first part is just the equilibrium (isotropic) Fermi distribution

$$f(k) = 1/(e^{(\mathcal{E}-\eta)/kT} + 1), \quad (2)$$

where η is the Fermi energy and $\mathcal{E} = \mathcal{E}(k)$ is the electron energy. The function $\mathcal{E}(k)$ is a nonparabolic function of $k = |\vec{k}|$ [see Ref. 1, Eq. (3)] and follows from the band structure given by Kane¹⁵ for zero spin-orbit splitting of the valence-band edge. The remaining part of the total distribution function is the perturbation distribution and is a small quantity, being of first order in the electric field. Thus, we write the following solution to Eq. (1) which has been shown to be exact for small \vec{F} and isotropic crystals¹:

$$f_T(\vec{k}) = f(k) + xg(k), \quad (3)$$

where x is the cosine of the angle between \vec{k} and \vec{F} , and the isotropic function $g(k)$ will be referred to as the perturbation distribution. The electron current is carried entirely by g . Although the current and electric field are vanishingly small so that Eq. (2) remains valid, the ratio of current density to electric field is finite and proportional to the electron mobility. Hence, we need only calculate the perturbation distribution g .

The Boltzmann equation is satisfied identically by f for zero electric field and an equilibrium distribution of the scattering centers. Thus Eq. (1) becomes, to first order in the electric field, an integrodifferential equation for g ,

$$\begin{aligned} xg \int [s(1-f') + s'f'] d\vec{k}' \\ = \int x'g'[s'(1-f) + sf] d\vec{k}' - x \frac{e}{\hbar} F \frac{\partial f}{\partial k}, \quad (4) \end{aligned}$$

where $g' = g(k')$, x' is the cosine of the angle between \vec{k}' and \vec{F} , and $F = |\vec{F}|$. The important point for the present formulation is that all of the integrals in Eq. (4) can be performed analytically for isotropic crystals. Equation (4) will then be reduced to a linear finite-difference equation^{5,6} which can easily be solved by numerical iteration. The differential-scattering rate $s(\vec{k}, \vec{k}')$ depends upon only k, k' , and the cosine X of the angle between \vec{k} and \vec{k}' . Thus, the integral term on the right-hand side of Eq. (4) is proportional to x since,¹⁶ in general,

$$\int x' \alpha(X) d\vec{k}' = x \int X \alpha(X) d\vec{k}', \quad (5)$$

where $\alpha(X)$ may be a function of X but not a function of x or x' . The $\alpha(X)$ is otherwise arbitrary and resembles the scattering integrand of Eq. (4). We have the following result, since Eq. (4) is homogeneous in x :

$$\begin{aligned} g \int [s(1-f') + s'f'] d\vec{k}' \\ = \int Xg'[s'(1-f) + sf] d\vec{k}' - \frac{e}{\hbar} F \frac{\partial f}{\partial k}. \quad (6) \end{aligned}$$

This equation is independent of all angular coordinates since X is one of the variables of the integration over \vec{k}' .

The differential-scattering rate s comprises inelastic (polar mode) scattering and elastic scattering (by acoustic modes and ionized centers) so that

$$s(\vec{k}, \vec{k}') = s_{\text{inel}}(\vec{k}, \vec{k}') + s_{\text{el}}(\vec{k}, \vec{k}'), \quad (7)$$

where the subscripts inel and el refer, respectively, to inelastic and elastic processes. For elastic processes, the arguments of the differential-scattering rate commute, according to the principle of detailed balance,¹⁷

$$s_{\text{el}}(\vec{k}, \vec{k}') = s_{\text{el}}(\vec{k}', \vec{k}). \quad (8)$$

These arguments (\vec{k} and \vec{k}') do *not* commute for inelastic processes, although we can still find an appropriate generalization of Eq. (8). There is only one inelastic process being considered here (polar-mode scattering) and the polar-phonon energy is $\hbar\omega_{\text{po}}$ where ω_{po} is assumed independent of the phonon wave vector. In this case, $s_{\text{inel}}(\vec{k}, \vec{k}')$ represents transitions from the state characterized by \vec{k} to \vec{k}' either by emission or by absorption of a phonon. For an *equilibrium* phonon distribution, the relative frequency of these two processes is simply the Boltzmann factor,

$$s_{ab}(\vec{k}', \vec{k}) = e^{-\hbar\omega_{po}/kT} s_{em}(\vec{k}, \vec{k}') , \quad (9)$$

where subscripts ab and em indicate absorption and emission. In the limit $\omega_{po} \rightarrow 0$, the scattering process becomes elastic and Eq. (9) is equivalent to Eq. (8). The equilibrium phonon occupation number of a polar mode is given by the Bose-Einstein distribution.

$$N_{po} = 1/(e^{\hbar\omega_{po}/kT} - 1) . \quad (10)$$

The probability of scattering by phonon absorption must be proportional to N_{po} so that, from Eq. (9), the probability of scattering by phonon emission must be proportional to $N_{po} + 1$.

The above results can be used to simplify Eq. (6) for the perturbation distribution. All elastic scattering processes (for which $k' = k$) combine to form a relaxation rate [see Eqs. (6) and (8)],

$$\nu_{e1} = \int (1 - X) s_{e1} d\vec{k}' . \quad (11)$$

We define the scattering-out rates by phonon absorption and emission, respectively:

$$N_{po}\lambda_0^+ = \int s_{ab}(\vec{k}, \vec{k}') d\vec{k}' , \quad (12)$$

$$(N_{po} + 1)\lambda_0^- = \int s_{em}(\vec{k}, \vec{k}') d\vec{k}' , \quad (13)$$

where Eq. (13) follows from Eqs. (9) and (12). The superscripts + and - indicate that the state \vec{k}' corresponds, respectively, to electron states of energy $\mathcal{E} + \hbar\omega_{po}$ and $\mathcal{E} - \hbar\omega_{po}$. Similarly, the scattering-in rates are

$$(N_{po} + 1)\lambda_i^+ = \int X s_{em}(\vec{k}', \vec{k}) d\vec{k}' , \quad (14)$$

$$N_{po}\lambda_i^- = \int X s_{ab}(\vec{k}', \vec{k}) d\vec{k}' . \quad (15)$$

Equations (12)–(15) define the functions $\lambda_0^+(k)$ and $\lambda_i^+(k)$ which are scattering-out and scattering-in rates aside from the phonon occupation numbers. These functions are evaluated in Sec. III.

The equation for the perturbation distribution Eq. (6) can be written as a finite-difference equation from Eqs. (6)–(15):

$$g = \frac{(N_{po} + f)\lambda_i^- g^- + (N_{po} + 1 - f)\lambda_i^+ g^+ - (e/\hbar) F \partial f / \partial k}{(N_{po} + 1 - f)\lambda_0^- + (N_{po} + f)\lambda_0^+ + \nu_{e1}} . \quad (16)$$

Equation (16) is solved numerically by iteration wherein the first approximation is to assume $g = 0$ and evaluate the right-hand side. This result just gives g in the relaxation approximation¹⁴ which assumes that scattering-in vanishes. The next iterated value of g uses the previously calculated g to evaluate the right-hand side of Eq. (16), etc. One notes that convergence proceeds exponentially so that three or four iterations ordinarily suffice for accuracies of $\sim 2\%$ in mobility. In addition, the convergence resembles the expected time-depen-

dent evolution of the electron distribution to a stepped-on electric field. If we were to add a large constant ν_0 to ν_{e1} and also add $\nu_0 g$ to the numerator of Eq. (16), we could show that the convergence would be slower. However, in this situation the successive iterations directly give the distribution function at successive instants in time.¹⁸ The time increments are equal to $1/\nu_0$, and ν_0 must be much greater than the remainder of the denominator in Eq. (16) as Rees¹⁸ has shown. Of course, ν_0 may even be negative¹⁹ so long as the denominator does not vanish, but then successive values of g do not correspond to time dependence. We conclude that Eq. (16) and the present method, derived from the Boltzmann equation, is equivalent to Rees's method in the low-field limit with all the integrals performed analytically. If we would include higher-order terms in Eq. (3), high-field time-dependent transport problems could be solved more efficiently than by the existing methods.^{18,20} Our present interest is, however, in low-field transport. Only minor modifications to Eq. (16) are needed in a calculation of thermoelectric power. The results are presented in the Appendix.

III. ELECTRON SCATTERING

The differential-scattering rates s and s' in Eq. (1), are proportional to the absolute squares of the Fourier coefficients of the scattering potentials, i. e., to the absolute squares of the matrix elements.¹⁴ For a nonparabolic conduction band with an electron wave-function admixture, the matrix elements are given in the literature.^{1,4,6} We will present only the results of the integrations indicated by Eqs. (11)–(15). There is one inelastic-scattering process, polar-mode scattering,^{10,11} and there are four elastic-scattering processes: (a) piezoelectric,^{7,8} (b) deformation-potential acoustic,⁹ (c) ionized-impurity,^{12,13} and (d) heavy-hole⁶ scattering. Screening of polar vibrations by free carriers²¹ produces a negligible over-all effect on transport and is not accounted for since fairly high free-carrier concentrations are required for screening effects to become important. In this case, the mobility is limited by ionized-center scattering anyway in which screening is correctly included.

The matrix element for polar-mode scattering in a band of the Kane type has been given by Ehrenreich.⁶ Substitution of the matrix element into Eqs. (12)–(15) and performance of the integrals leads to the following results:

$$\lambda_0^+(k) = \beta^* \left((A^*)^2 \ln \left| \frac{k^* + k}{k^* - k} \right| - A^* c c^* - a a^* c c^* \right) , \quad (17)$$

$$\lambda_i^+(k) = \beta^* \left(\frac{k^{*2} + k^2}{2k^* k} (A^*)^2 \ln \left| \frac{k^* + k}{k^* - k} \right| - (A^*)^2 - \frac{1}{3} c^2 c^{*2} \right) . \quad (18)$$

The λ_0^+ and λ_i^- follow by replacement of the superscripts (+) in Eqs. (17) and (18) by superscripts (-). The k -dependent quantities a and c are the respective linear-expansion coefficients of the electron wave function consisting of s - and p -type wave functions.^{1,15} For a parabolic band, $a = 1$, $c = 0$, and the wave function is purely s type:

$$A^+ = aa^+ + [(k^+ + k^2)/2k^+k]cc^+, \quad (19)$$

$$\beta^+ = (e^2\omega_{po}md^*/4\pi\hbar^2k)(1/\epsilon_\infty - 1/\epsilon_0), \quad (20)$$

where ϵ_0 and ϵ_∞ are, respectively, the low- and high-frequency dielectric permittivities. The quantity md^* [see Ref. 1, Eq. (5)] corresponds to the local effective mass in energy space. For a parabolic band where $a = 1$ and $c = 0$, we find $A^+ = 1$ and $md^+ = m^*$, the effective mass in the usual sense. Evidently, Eqs. (17) and (18) simplify considerably for a parabolic band. We do not, however, assume a parabolic conduction band in this paper.

The relaxation rate ν_{e1} , in Eq. (16), for elastic scattering consists of the sum of relaxation rates for the individual scattering mechanisms,

$$\nu_{e1} = \nu_{pe} + \nu_{ac} + \nu_{ii}, \quad (21)$$

where subscripts pe and ac correspond, respectively, to piezoelectric and deformation-potential acoustic-mode scattering. ν_{ii} represents scattering by fixed ionized centers as well as electron-hole scattering since the majority of holes are heavy holes which can be considered fixed during the scattering event.⁶ The relaxation rate for deformation-potential scattering in a nonparabolic band follows from Eq. (11) and the matrix element,¹

$$\nu_{ac} = (e^2\kappa TE_1^2mdk/3\pi\hbar^3c_1)(3 - 8c^2 + 6c^4), \quad (22)$$

where E_1 is the acoustic deformation potential and c_1 is the spherically averaged elastic constant^{1,22} for longitudinal acoustic modes. The acoustic-mode scattering rate, Eq. (22), is approximately proportional to electron speed and leads to a $T^{-3/2}$ mobility dependence.

Piezoelectric scattering has been discussed previously.^{1,2} The relaxation rate is

$$\nu_{pe} = (e^2\kappa TP^2md/6\pi\hbar^3\epsilon_0k)(3 - 6c^2 + 4c^4), \quad (23)$$

where P is the (dimensionless) spherically averaged electromechanical coupling coefficient discussed by Hutson.²³ We refer to P as the piezoelectric coefficient. For the sphalerite structure possessed by InSb, InAs, and InP, the piezoelectric coefficient becomes

$$P^2 = e_{14}^2(12/c_t + 16/c_t)/35\epsilon_0, \quad (24)$$

where c_t is the spherically averaged elastic constant^{1,22} for transverse acoustic modes and e_{14} is the single independent element of the piezoelectric tensor. In general, transverse acoustic modes

contribute three to four times more scattering than longitudinal acoustic modes. For an ideally isotropic crystal whose atoms interact only by central forces,²⁴ $(16/c_t)/(12/c_t) = 4$ which is approximately true for InSb, InAs, and InP (see Table I). Piezoelectric scattering yields a mobility nearly proportional to $T^{-1/2}$.

Electron scattering by ionized centers, i. e., fixed ionized impurities and mobile heavy holes, has been discussed by Brooks,¹² Herring,¹² and Dingle.¹³ Heavy-hole scattering is essentially equivalent to fixed ionized-impurity scattering⁶ except that the screening length for the Coulomb potential is complicated by the presence of two types of free carriers.¹³ Strictly speaking, we should account for the fact that screening of fixed centers occurs via both species, electrons and holes, whereas screening of holes is due mainly to electrons alone. However, provided the Born approximation is valid, the mobility turns out to be insensitive to whether we assume only screening by electrons or the more complicated case above. In any case, such a mixed manner of screening does not prevail over a significant temperature range since hole concentration is ordinarily a strong function of temperature (excluding p material). Therefore, we treat all holes as being heavy and uninvolved in screening. The relaxation rate follows as⁴

$$\nu_{ii} = (e^4Nmd/8\pi\epsilon_0^2\hbar^3k^3)[D \ln(1 + 4k^2/\beta^2) - B], \quad (25)$$

TABLE I. Material parameters.

Material	InSb	InAs	InP
Effective mass at Γ_{1c} at 0 °K m^*/m	0.0155	0.025	0.072 ^a
Effective-mass energy gap at 0 °K \mathcal{E}_g^* (eV)	0.265 ^b	0.46 ^b	1.42 ^b
Energy-gap temperature coefficient $3\alpha \left(\frac{\partial \mathcal{E}_g}{\partial P}\right)_T / K \left(\frac{eV}{^\circ K}\right) (10^{-4})$	0.97	0.69	0.41
Low-frequency dielectric constant ϵ_0/ϵ	17.64	14.54	12.38
High-frequency dielectric constant ϵ_∞/ϵ	15.75	12.25 ^c	9.55
Polar-phonon Debye temperature T_{po} (°K)	274 ^d	337 ^d	497 ^e
Acoustic-deformation potential E_1 (eV)	9.5	11.5	14.5
Longitudinal elastic constant c_l (10^{10} N/m ²)	7.89	9.98	12.10
Transverse elastic constant c_t (10^{10} N/m ²)	2.42	3.14	3.65
Piezoelectric coefficient P	0.027	0.017	0.013

^aReferences 61 and 62.

^dReference 29.

^bReference 38, p. 122.

^eReference 63.

^cReference 46.

where the total number of ionized scattering centers N is related to the hole concentration p , the ionized donor-impurity concentration N^+ , and the ionized acceptor-impurity concentration N^- ,

$$N = N^+ + N^- + p, \quad (26)$$

$$D = 1 + 2\beta^2 c^2 / k^2 + 3\beta^4 c^4 / 4k^4, \quad (27)$$

$$B = [4k^2 + 8(\beta^2 + 2k^2)c^2 + (3\beta^4 + 6\beta^2 k^2 - 8k^4)c^4 / k^2] / (\beta^2 + 4k^2). \quad (28)$$

The screening length is $1/\beta$, where β , for Fermi-Dirac statistics and a nonparabolic band, is related to the Fermi energy η of Eq. (2)¹³:

$$\beta^2 = (e^2 / \pi^2 \epsilon_0 \kappa T) \int_0^\infty k^2 f(1-f) dk. \quad (29)$$

To avoid having to discuss the valence band in detail, the experimental values of intrinsic electron and hole concentrations are used in calculations of the Fermi level for pure materials. Given the free-electron concentration n , for intrinsic or extrinsic cases, the Fermi level is obtained from the following formula¹³:

$$n = \int_0^\infty (k/\pi)^2 f dk. \quad (30)$$

It has been pointed out⁴ that Eq. (25) assumes binary-scattering events, an assumption which fails at sufficiently low temperatures ($\approx 20^\circ\text{K}$, depending upon the impurity concentrations). If μ_{ii} is the mobility due to ionized-center scattering, Eq. (25) is valid in this respect if the following criterion is satisfied⁴:

$$\mu_{ii}^2 > \epsilon_0 / m^* n. \quad (31)$$

This criterion as well as the Born approximation is satisfied for all results presented in Sec. IV.

IV. RESULTS

From the perturbation distribution of Eq. (16), the drift mobility is calculated by numerical integration of the following formula¹:

$$\mu = \frac{\hbar}{3m} \int_0^\infty \frac{k^3 g}{F d} dk / \int_0^\infty k^2 f dk. \quad (32)$$

The thermoelectric power discussed in the Appendix is calculated in a similar fashion.

Drift mobility and thermoelectric power are calculated with no adjustable parameters. All parameters necessary for characterizing the material have been determined by experiments independent of transport properties themselves. Hence, good agreement between theory and experiment regarding transport quantities should provide a trustworthy confirmation of the microscopic description.

The various material parameters for InSb, InAs, and InP are presented in Table I. A discussion of the derivation of Table I follows first for InSb.

A. InSb

Shubnikov-de Haas experiments have shown the Γ_{1c} minimum of InSb to be very nearly spherical.²⁵ The effective mass at the conduction-band edge for zero temperature has been reviewed by Madelung²⁶; Cardona²⁷ calculated $m^* = 0.0152m$. We take $m^* = 0.0155$ at 0°K and allow m^* to vary with temperature according to Kane's band theory for zero spin-orbit splitting,^{1,15}

$$m^* = m / (1 + \mathcal{O}^2 / \mathcal{E}_g^*), \quad (33)$$

where \mathcal{O} is a matrix element for conduction-valence-band interactions, and \mathcal{E}_g^* is the effective-mass energy gap given by Ehrenreich,⁶

$$\mathcal{E}_g^*(T) = \mathcal{E}_g^*(0^\circ\text{K}) - 3\alpha T \left(\frac{\partial \mathcal{E}_g}{\partial P} \right)_T / K, \quad (34)$$

where the thermal-expansion coefficient α , the pressure-rate coefficient of the energy gap $(\partial \mathcal{E}_g / \partial P)_T$, and the compressibility K , are assigned their room-temperature values.²⁸ Since the mobility is sensitive to $\epsilon_0 - \epsilon_\infty$ which appears in Eq.

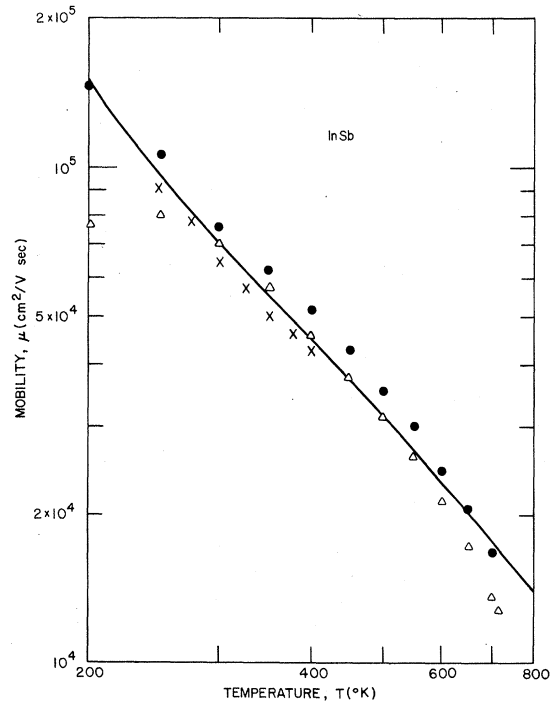


FIG. 1. Electron-drift mobility vs temperature of pure intrinsic InSb. The calculated curve agrees with experiment up to 700°K , just below the melting point at $\sim 780^\circ\text{K}$. Experimental data are Hall mobilities: Δ , Ref. 32; \bullet , Ref. 33; \times , Ref. 35.

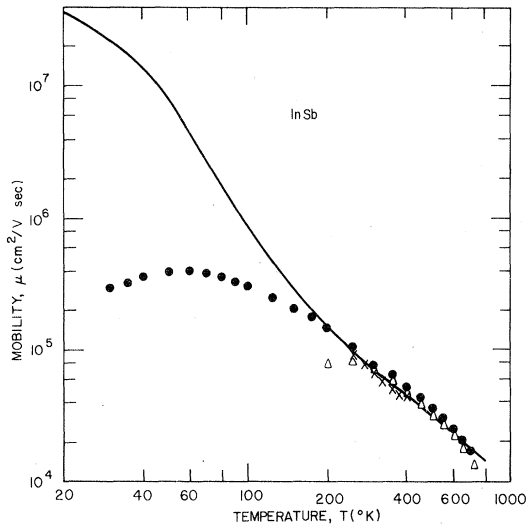


FIG. 2. Intrinsic mobility of InSb over a wide temperature range. The data are the same as in Fig. 1. and show diminished mobilities at low temperatures because of impurity scattering.

(20), we rederive the dielectric constants from the Lyddane-Sachs-Teller relationship. The directly measured values of ϵ_0 and ϵ_∞ are given by Seraphin and Bennett.²⁸ We use the average of the values reported by Hass²⁹ for the longitudinal and transverse optical-phonon frequencies at Γ . The polar-phonon Debye temperature $T_{po} = \hbar\omega_{po}/k$, from Hass and the dielectric constants are, to good approximation,² assumed constant. Elastic constants required for evaluation of the spherically averaged elastic constants c_l and c_t of Eqs. (22) and (24) appear in the text by Madelung²⁶ and we assign

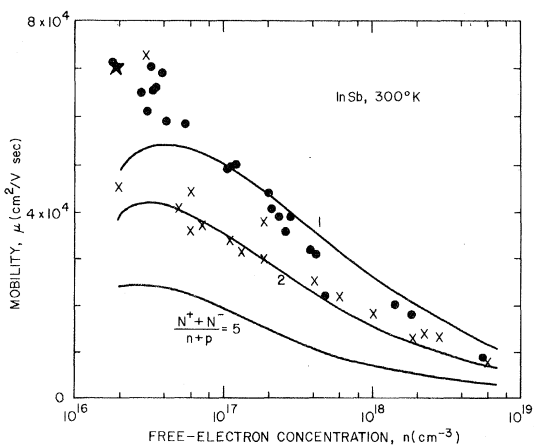


FIG. 3. Mobility vs free-electron concentration in InSb at 300 °K for compensation ratios of 1, 2, and 5. The star near the upper left-hand corner represents pure material. Experimental data are Hall mobilities: ●, Ref. 37; ×, Ref. 38.

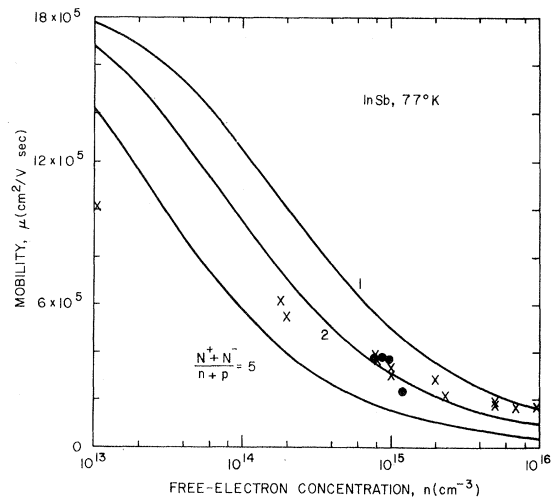


FIG. 4. Mobility vs free-electron concentration in InSb at 77 °K for compensation ratios of 1, 2, and 5. Experimental data are Hall mobilities: ●, Ref. 33; ×, Ref. 38.

these quantities their room-temperature values. The acoustic-deformation potential for InSb is taken to be identical to that for the isoelectronic system CdTe, i. e., $E_1 = 9.5$ eV.² The piezoelectric constant, e_{14} of Eq. (24), has been measured to be 0.071 C/m² at room temperature,³⁰ in good agreement with theory.³¹

InSb of sufficient purity to exhibit intrinsic transport below about 200 °K is not yet available. Hence, Fig. 1 presents electron-drift mobility for intrinsic material from 200 °K upward to the melting point (~ 780 °K). The curve is calculated from the parameters listed in Table I and from intrinsic electron and hole concentrations determined experimentally from Hall measurements.³²⁻³⁴ The data points^{32,33,35} represent various experimental Hall-mobility results. Polar-mode scattering dominates below room temperature. Electron-hole scattering dominates above room temperature. The agreement from 200 to 700 °K is quite good aside from evidence of ionized-impurity scattering below 300 °K for one sample³² indicated by open triangular data points. At higher temperatures, the experiments in mobility which is not shown by the calculated curve. Although one might question the validity of neglecting spin-orbit splitting in the band structure here, it seems more likely that the discrepancy is due to the onset of multivalley conduction above 700 °K. This suspicion receives added weight from the fact that similar behavior is evident in InP (see Fig. 13), GaAs,⁴ and CdTe.² In addition, the L_{1c} minima of the conduction band are only³⁶ 0.40–0.55 eV above the Γ_{1c} minimum and are expected to become accessible to electrons at these high temperatures. The

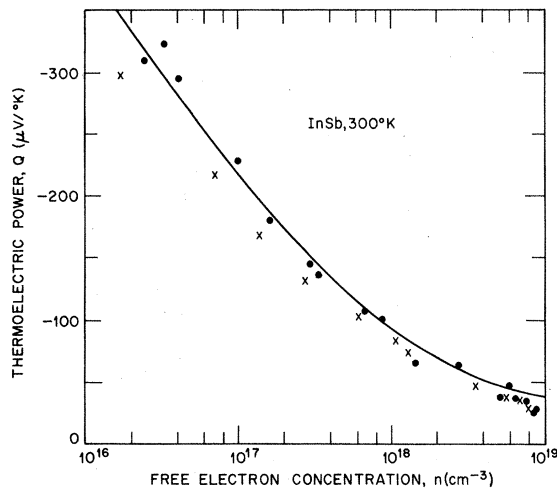


FIG. 5. Thermoelectric power vs free-electron concentration in InSb. Agreement of the calculated curve with the more recent data of Filipchenko and Nasledov (Ref. 39) is excellent except for $n > 6 \times 10^{18} \text{ cm}^{-3}$ where multivalley conduction appears. Experimental data: ●, Ref. 39; ×, Ref. 40.

calculated curve in Fig. 2 applies also to pure intrinsic InSb. Below 60°K , deformation-potential scattering and piezoelectric scattering are the dominant forms of lattice scattering. The approximate $T^{-1/2}$ mobility dependence near 20°K signals the dominance of piezoelectric scattering.

In many experimental situations, impurity concentrations are sufficiently high to limit the mobility. One can then use the mobility and free-electron concentration determined by Hall measurements to calculate the donor and acceptor concentrations from Figs. 3 and 4. The electron-drift mobility at 300°K , Fig. 3, and 77°K , Fig. 4, is plotted for several values of the compensation ratio $(N^+ + N^-)/(n + p)$. The compensation ratio equals zero for pure intrinsic material. The curve in Fig. 3 for a compensation ratio of unity displays a maximum value at $n \approx 4 \times 10^{16} \text{ cm}^{-3}$ because the use of unity for the compensation ratio ensures the presence of some acceptor impurities. The point appearing in Fig. 3 as a star, at $\mu = 70\,400 \text{ cm}^2/\text{Vsec}$ and $n = 1.9 \times 10^{16} \text{ cm}^{-3}$, represents the mobility and intrinsic electron concentration at 300°K for perfectly pure InSb. Agreement with experiment^{37,38} in Fig. 3 is reasonable, although above $n = 6 \times 10^{18}$ the Fermi level rises 0.35 eV above the conduction-band edge and one must be cautious of multivalley conduction. Figure 4 displays the expected experimental behavior^{33,38} wherein the compensation ratio increases with decreasing free-electron concentration due to the presence of a fixed number of acceptor impurities.

Figure 5 presents thermoelectric power vs free-electron concentration. The curve is calculated for

zero acceptor-impurity concentration and the two sets of data points^{39,40} are experimental. Agreement with the more recent data of Filipchenko and Nasledov³⁹ leaves little to be desired except for $n > 6 \times 10^{18} \text{ cm}^{-3}$. As mentioned above, we suspect some amount of multivalley conduction at these high densities.

Thermoelectric power^{32,41,42} vs temperature appears in Fig. 6 for intrinsic InSb. Near the melting point ($\sim 780^\circ\text{K}$), the experimental data⁴¹ fall well below the calculated curve (see also Fig. 1 above). Perhaps the loss of long-range crystalline order is partly to blame. However, since similar behavior develops at room temperature and high n (Fig. 5), it seems that multivalley conduction again plays the dominant role in the discrepancy between theory and experiment near the melting point. The remainder of the data^{32,42} below 700°K agree fairly well with the calculation.

B. InAs

Regarding InAs, Madelung²⁶ reviews the effective mass at the conduction-band edge and concludes that $m^*/m = 0.023$ to 0.027 . We take $m^*/m = 0.025$ at zero temperature in agreement with Summers and Smith⁴³ who find $m^*/m = 0.022$ and 0.024 at 300 and 77°K , respectively, from Faraday rotation experiments. We allow m^* and δ_g^* to vary with temperature according to Eqs. (33) and (34). The elastic constants, thermal-expansion coefficient, and pressure-rate coefficient of the energy gap are assigned their room-temperature values.²⁶ Unfortunately, a series of corroborating phonon data

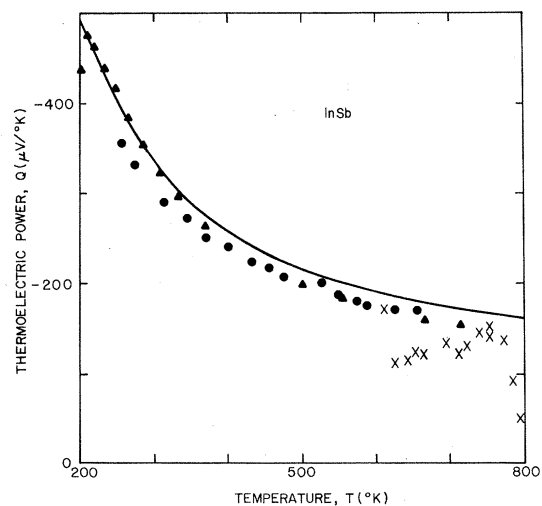


FIG. 6. Thermoelectric power vs temperature in InSb. Agreement between the calculated curve and experiment is fair except above 700°K , just below the melting point at $\sim 780^\circ\text{K}$, where multivalley conduction occurs. Experimental data: ●, Ref. 32; ×, Ref. 41; ▲, Ref. 42.

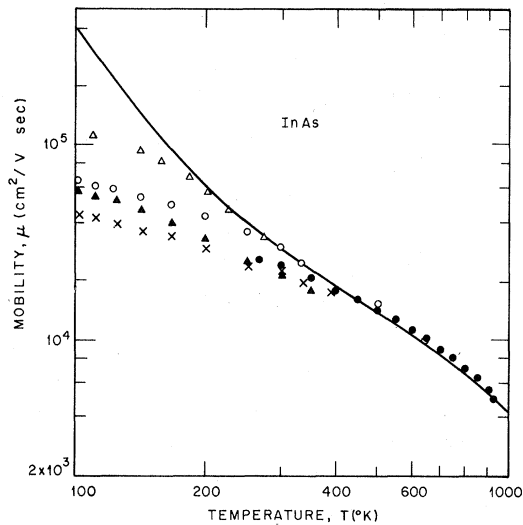


FIG. 7. Electron-drift mobility vs temperature of pure intrinsic InAs. Agreement between the calculated curve and experiment obtains up to the highest temperatures studied. Impurity scattering dominates the data below room temperature. Experimental data are Hall mobilities: ○, Ref. 47; ●, Ref. 48; ▲, Ref. 49; ×, Ref. 50; △, Ref. 51.

by several methods (e.g., transmission, reflection, Raman scattering) is not available at this time for use in a derivation of the dielectric constants. Respective values for ϵ_∞ and ϵ_0 have been reported as⁴⁴ 11.8 and 14.55 as well as⁴⁵ 11.7 and 14.5. The reported longitudinal and transverse optical-phonon frequencies²⁹ yield, through the Lyddane-

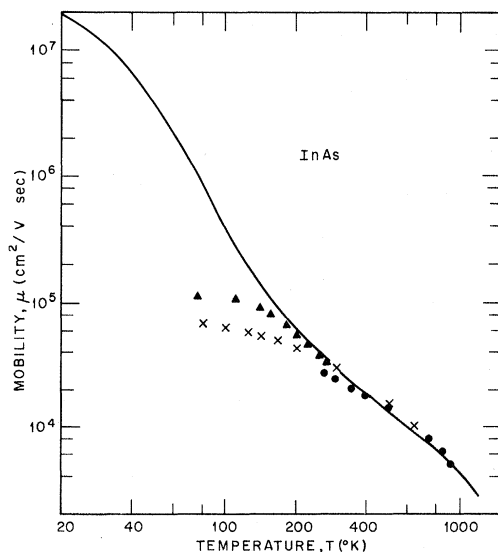


FIG. 8. Intrinsic mobility of InAs. Piezoelectric and deformation-potential scattering dominate below 80 °K. Experimental data are Hall mobilities: ×, Ref. 47; ●, Ref. 48; ▲, Ref. 51.

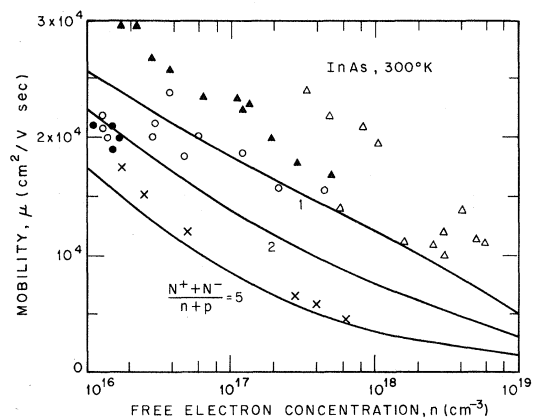


FIG. 9. Mobility vs free-electron concentration in InAs at 300 °K for compensation ratios of 1, 2, and 5. An accurate comparison of the calculated curves with experiment is not possible, although better agreement appears to exist for the more recent data indicated as open and closed circles. Experimental data are Hall mobilities: ○, Ref. 49; ●, Refs. 51 and 55; △, Ref. 53; ▲, Ref. 54; ×, Ref. 56.

Sachs-Teller relationship, $\epsilon_0 = 14.54$ and $\epsilon_\infty = 11.74$. However, these values lead to a room-temperature mobility $\sim 20\%$ too low, as indicated by several experiments (see below). Hence, we use $\epsilon_0 = 14.54$, as above, and $\epsilon_\infty = 12.25$ reported by Moss.⁴⁶ Additional experimental data are needed to confirm these numbers. Approximate correction of the longitudinal optical frequency²⁹ to room temperature leads to the value of T_{p0} shown in Table I. The acoustic-deformation potential is assigned the value found for the isoelectronic system CdSe, i.e.,

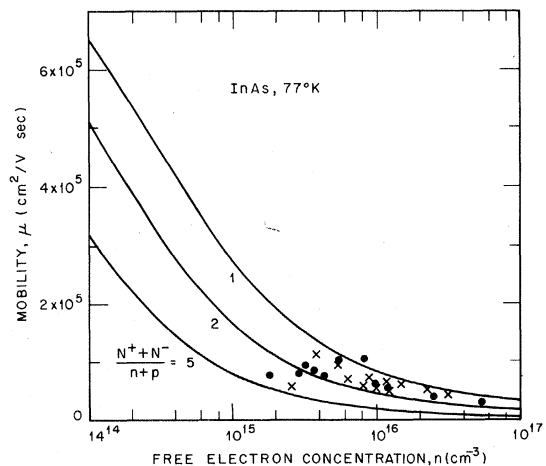


FIG. 10. Mobility vs free-electron concentration in InAs at 77 °K for compensation ratios of 1, 2, and 5. Sufficiently pure materials for comparisons at low n are not yet available. Experimental data are Hall mobilities: ●, Refs. 49 and 57; ×, Refs. 51 and 55.

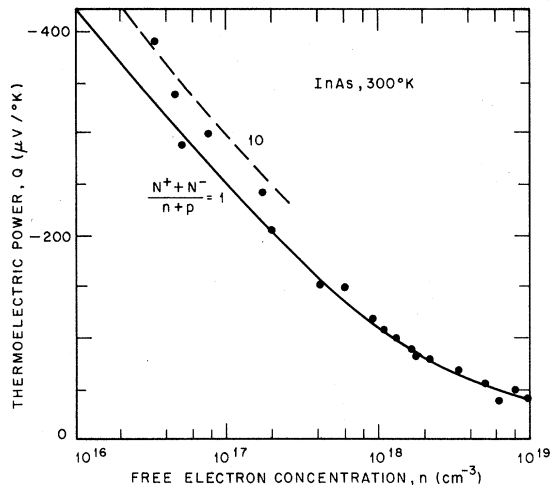


FIG. 11. Thermoelectric power vs free-electron concentration in InAs. Agreement between the calculated curves and experiment (Ref. 58) is excellent, and the comparison indicates the expected higher compensation ratios for small n .

$E_1 = 11.5$ eV.² The measured piezoelectric constant³⁰ $e_{14} = 0.045$ C/m² agrees only qualitatively with the theoretically predicted value of³¹ 0.022 C/m². The experimental value is used for the present work.

The solid curve in Fig. 7 is calculated for pure intrinsic InAs. Intrinsic electron and hole concentrations are assigned their experimental values.^{47, 48} The experimental data points⁴⁷⁻⁵¹ represent Hall mobilities. Below 200°K, the experimental mobility is limited by ionized-impurity scattering. Good

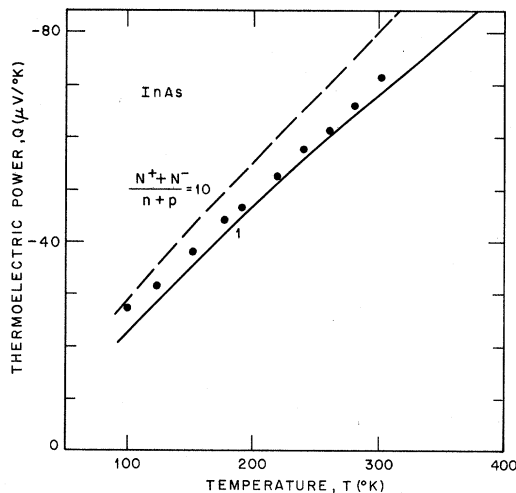


FIG. 12. Thermoelectric power vs temperature in degenerate extrinsic InAs. $n = 3 \times 10^{18}$ cm⁻³ at room temperature (Ref. 58). The increased values of Q over the calculated curve below 200°K probably are due to carrier freeze out.

agreement is evident at higher temperatures up to 900°K. The next-lowest conduction-band minima (of unknown symmetry) are far removed⁵² (~ 1.35 eV) from the Γ_{1c} minimum under consideration here. Hence, the present description should not be complicated by multivalley conduction even at the melting point (~ 1200 °K). Figure 8 shows the calculated mobility at lower temperatures where piezoelectric scattering and deformation-potential scattering become noticeable below 80°K. The earlier experimental data^{53, 54} (open and closed triangles) shown on Fig. 9 for 300°K Hall mobilities tend to fall somewhat higher than the calculated curves. Better agreement exists for the remaining data.^{49, 51, 55, 56} At 77°K, Fig. 10 shows that experiment^{49, 51, 55, 57} and theory agree quite well. For the higher free-electron concentrations shown in Fig. 10, the experimental compensation ratio is indicated to lie between unity and 2. Data⁵⁸ on thermoelectric power vs free-electron concentration compare well to the calculated curve in Fig. 11. At low values of n , high compensation ratios are experimentally common. For this reason, the dashed curve for a compensation ratio of 10 is presented in Fig. 11. Note the good agreement for $n = 1 \times 10^{19}$ cm⁻³, where the Fermi level lies 0.35 eV above the conduction-band edge.

Kesamanly *et al.*⁵⁸ have measured thermoelectric power vs temperature on extrinsic samples of InAs. The free-electron concentration is stated by the authors at only room temperature. Data from one such sample with $n = 3 \times 10^{18}$ cm⁻³ at room tempera-

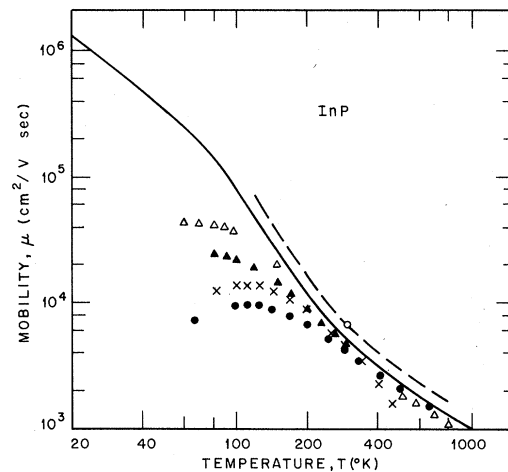


FIG. 13. Electron-drift mobility vs temperature of pure intrinsic InP. At low temperatures the experimental data are limited by impurity scattering. Agreement is favorable from 200°K to 800°K, above which multivalley conduction occurs. The dashed curve is calculated from $m^*/m = 0.06$ which is apparently too small. Experimental data are Hall mobilities: ●, Ref. 65; △, Ref. 66; ○, Ref. 68; ▲, Ref. 69; ×, Ref. 70.

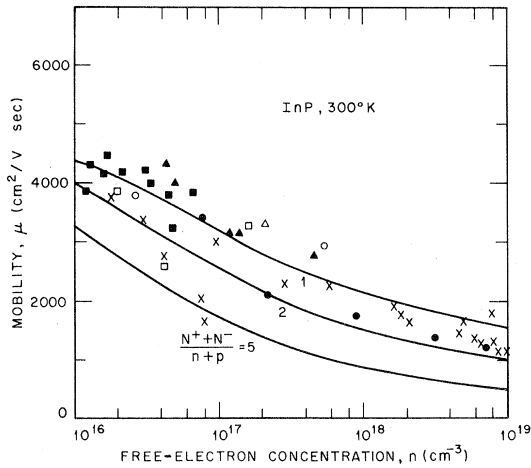


FIG. 14. Mobility vs free-electron concentration in InP at 300°K for compensation ratios of 1, 2, and 5. The curves are calculated and the data points are experimental Hall mobilities: ○, Ref. 69; ●, Ref. 71; ×, Ref. 72; ▲, Ref. 73; △, Ref. 74; □, Ref. 75; ■, Ref. 76.

ture are plotted in Fig. 12. The curves are calculated under the assumption that the free-electron concentration maintains its room-temperature value over the entire temperature range. A decrease in n at lower temperature could account for the somewhat higher experimental thermoelectric power values below 200°K. The agreement is good at higher temperatures for a compensation ratio of unity which is characteristic of highly doped extrinsic material.

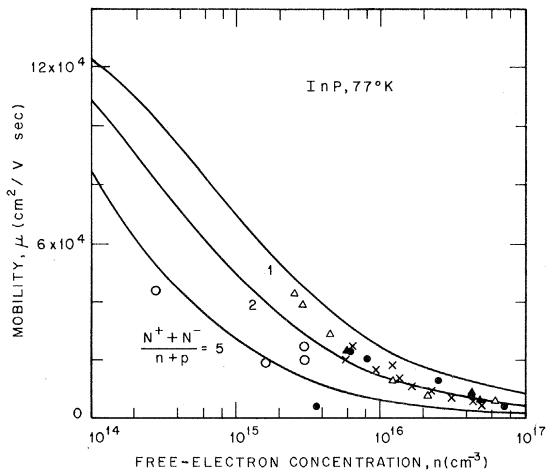


FIG. 15. Mobility vs free-electron concentration in InP at 77°K for compensation ratios 1, 2, and 5. Good agreement is evident between the calculated curves and the experimental Hall mobility data: △, Ref. 66; ●, Ref. 69; ▲, Ref. 73; ×, Ref. 76; ○, Ref. 77.

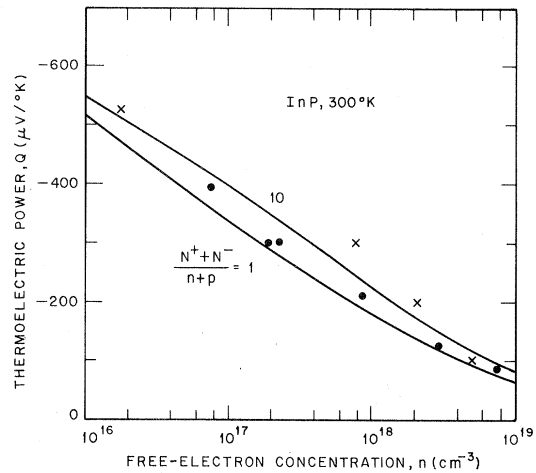


FIG. 16. Thermoelectric power vs free-electron concentration in InP. The more recent experimental data (circles) of Kesamanly *et al.* (Ref. 71) show better agreement with the calculated curves than do the earlier data (Ref. 78).

C. InP

For InP, the thermal energy gap at 0°K is given by Hilsun and Rose-Innes,³⁸ and the spin-orbit splitting $\Delta_0 = 0.11$ eV of the valence-band edge has been measured by Cardona *et al.*⁵⁹ Using⁶⁰ $\phi^2 = 23$ eV for the matrix element of Eq. (33) and including spin-orbit splitting in the effective-mass formula¹⁵

$$m/m^* = 1 + \frac{1}{3}\phi^2 [2/\mathcal{E}_g^* + 1/(\mathcal{E}_g^* + \Delta_0)], \quad (35)$$

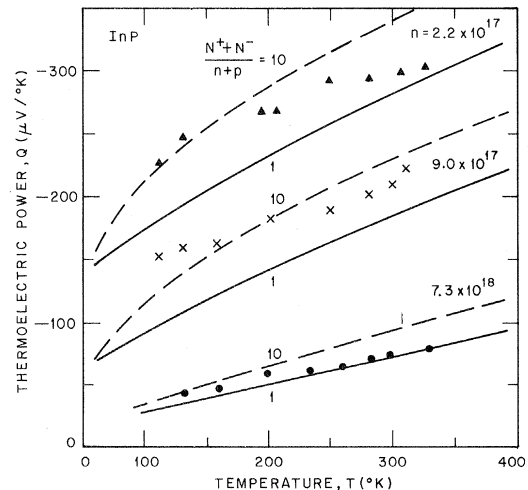


FIG. 17. Thermoelectric power vs temperature of extrinsic InP. The curves are calculated for the stated (Ref. 71) room-temperature values of n . Decreasing free-electron concentrations at lower temperatures are the probable source of difference between the curves and the data (Ref. 71) since agreement at 300°K is fair.

we calculate $m^*/m = 0.06$. This value of m^* is somewhat smaller than the experimentally determined values and leads to calculated mobilities which are noticeably higher than is suggested by several experiments (see Fig. 13, dashed curve). Perhaps the matrix element ρ is diminished slightly by the influence of higher bands (e. g., Γ_{15c}). In any case, we choose $m^*/m = 0.072$ at 0°K which nearly agrees with various experimental results.^{61,62} The high-frequency dielectric constant has been reported as²⁸ $\epsilon_\infty = 9.57$ and⁶³ $\epsilon_\infty = 9.52$. We take $\epsilon_\infty = 9.55$ and calculate ϵ_0 from the Lyddane-Sachs-Teller relationship. The ratio of the longitudinal and transverse optical-phonon frequencies agrees to $\frac{1}{2}\%$ for data given by Hass²⁹ and by Hilsun *et al.*⁶³ We find, from the data of Hilsun *et al.*, $\epsilon_0 = 12.38$. The acoustic-deformation potential is assigned the value found for the isoelectronic system CdS, i. e., $E_1 = 14.5 \text{ eV}$.² Kleinman⁶⁴ reports the piezoelectric constant $e_{14} = 0.035 \text{ C/m}^2$ which agrees well with the theoretically predicted value³¹ (0.039 C/m^2). Experimental data by Folberth and Weiss⁶⁵ provide intrinsic electron and hole concentrations.

Figure 13 shows the calculated drift mobility vs temperature for intrinsic InP. Piezoelectric scattering dominates below 60°K . Above 800°K , multivalley conduction becomes important as indicated by the data (open triangles) of Galavanov and Siukaev.⁶⁶ These authors measure $\mu_H = 740 \text{ cm}^2/\text{V sec}$ at 1000°K , whereas the calculated drift mobility is $985 \text{ cm}^2/\text{V sec}$. James *et al.*⁶⁷ report the Γ_{1c} to L_{1c} separation as 0.61 eV . Agreement with the various⁶⁵⁻⁷⁰ experiments is reasonable from 200 to 800°K . Below 200°K , the experimental data are dominated by ionized-impurity scattering. The solid curve corresponds to $m^*/m = 0.072$; the dashed curve to 0.06 . The latter value is evidently too small. The mobility vs free-electron concentration at^{69,71-76} 300 and^{66,69,73,76,77} 77°K appears in Figs. 14 and 15. Thermoelectric power vs free-electron concentration given in Fig. 16 agrees better with the more recent data (circles) of Kesamanly *et al.*⁷¹ than with earlier results.⁷⁸ The comparison between theory and experiment⁷¹ in Fig. 17 is satisfactory near room temperature. Values for n at temperatures lower than 300°K were not given in Ref. 71, but it seems likely that decreasing electron concentrations are responsible for the tendency of the data to exceed the calculated thermoelectric power at lower temperatures.

In conclusion, the present description of InSb is adequate for temperatures as high as 700°K , beyond which multivalley conduction is important. For InAs, conduction in the Γ_{1c} minimum should be dominant up to the melting point ($\sim 1200^\circ\text{K}$). Multivalley conduction in InP becomes evident above 800°K . Lattice scattering in the present formulation is expected to be accurately described at least

down to $\sim 2^\circ\text{K}$ (see Ref. 2). The generally good agreement between theory and experiment attests to the accuracy of the present model as well as to the material parameters derived herein. Conduction-band nonparabolicity and electron-hole scattering are important in InSb above 250°K . Above 450°K , the effects of degeneracy in InSb become noticeable.

ACKNOWLEDGMENTS

The author appreciates the encouragement provided by Dr. F. H. Blecher and by Dr. J. A. Copeland. Reference 72 was graciously supplied by Dr. H. Quesser.

APPENDIX

The current density \vec{J} in an isotropic crystal is proportional to the driving forces for small driving forces. The driving forces are the electric field \vec{F} , the gradient of the Fermi energy $\nabla\eta$, and the temperature gradient ∇T . For mobile charges with charge q , the quantity $-\nabla\eta/q$ is equivalent to an electric field. Thermoelectric power is defined, when $\vec{J} = 0$, as (taking all gradients along the z direction)

$$Q = F \left/ \frac{\partial T}{\partial z} \right. . \quad (\text{A1})$$

Hence, the current density, in general, is

$$\vec{J} = \sigma (\vec{F} - \nabla\eta/q - Q\nabla T) , \quad (\text{A2})$$

where σ is the conductivity. Thermoelectric power Q has the same algebraic sign as q . When $\vec{J} = 0$, Eq. (A2) simply returns the definition Eq. (A1), since $\nabla\eta = 0$ in that case. Therefore, we must derive Q theoretically from the short-circuit current, i. e., when $\vec{F} = 0$. From Eq. (A2) with $\vec{F} = 0$,

$$Q = - \left(\frac{1}{q} \frac{\partial\eta}{\partial z} + \frac{J}{\sigma} \right) \left/ \frac{\partial T}{\partial z} \right. . \quad (\text{A3})$$

Poisson's equation $\nabla \cdot \vec{F} = 0$ yields

$$\frac{\partial\eta}{\partial z} \left/ \frac{\partial T}{\partial z} \right. = \frac{\eta}{T} - \int_0^\infty k^2 f(1-f) \frac{\mathcal{E}}{T} dk \left/ \int_0^\infty k^2 f(1-f) dk \right. . \quad (\text{A4})$$

Combining Eqs. (A3) and (A4), we have

$$Q = \frac{\kappa}{q} \left[\frac{-\eta}{\kappa T} + \int_0^\infty k^2 f(1-f) \frac{\mathcal{E}}{\kappa T} dk \left/ \int_0^\infty k^2 f(1-f) dk \right. - qJ \left(\sigma \kappa \frac{\partial T}{\partial z} \right)^{-1} \right] . \quad (\text{A5})$$

The short-circuit current J is calculated from the perturbation distribution g of Eq. (16) with the following changes: There is no electric field in this case, and the term $[(e/\hbar)F\partial f/\partial k]$ in Eq. (16) must

be replaced by

$$\hbar k \frac{\partial T}{\partial z} (mdT)^{-1} f(1-f) \times \left(\frac{\mathcal{E}}{kT} - \int_0^\infty k^2 f(1-f) \frac{\mathcal{E}}{kT} dk \right) / \left(\int_0^\infty k^2 f(1-f) dk \right), \quad (\text{A6})$$

where m is the electron mass in vacuum and d

[given in Ref. 1, Eq. (5)] accounts for conduction-band nonparabolicity. The short-circuit current is used in Eq. (A5) for the calculation of thermoelectric power for given concentrations of free electrons and ionized impurities. No phonon-drag effects are included since the phonon distribution is assumed to be at equilibrium. It is apparent from Eq. (A6) that one must know the drift mobility ($= \sigma/en$) in order to calculate thermoelectric power.

- ¹D. L. Rode, Phys. Rev. B 2, 1012 (1970).
²D. L. Rode, Phys. Rev. B 2, 4036 (1970).
³C. M. Wolfe, G. E. Stillman, and J. O. Dimmock, J. Appl. Phys. 41, 504 (1970).
⁴D. L. Rode and S. Knight, Phys. Rev. (to be published).
⁵D. J. Howarth and E. H. Sondheimer, Proc. Roy. Soc. (London) A219, 53 (1953).
⁶H. Ehrenreich, J. Phys. Chem. Solids 2, 131 (1957); 9, 129 (1959).
⁷H. J. G. Meijer and D. Polder, Physica 19, 255 (1953).
⁸W. A. Harrison, Phys. Rev. 101, 903 (1956).
⁹J. Bardeen and W. Shockley, Phys. Rev. 80, 72 (1950).
¹⁰H. B. Callen, Phys. Rev. 76, 1394 (1949).
¹¹H. Frohlich, Advan. Phys. 3, 325 (1954).
¹²H. Brooks, Advan. Electron. Electron Phys. 7, 85 (1955); C. Herring (unpublished).
¹³R. B. Dingle, Phil. Mag. 46, 831 (1955).
¹⁴J. M. Ziman, *Electrons and Phonons* (Oxford U. P., London, 1967), p. 264.
¹⁵E. O. Kane, J. Phys. Chem. Solids 1, 249 (1957).
¹⁶E. Jahnke and F. Emde, *Tables of Functions* (Dover, New York, 1945), p. 115.
¹⁷W. Heitler, *The Quantum Theory of Radiation* (Oxford U. P., London, 1954), Appendix 5. Note that the differential-scattering rates include summations over spin directions implicitly.
¹⁸H. D. Rees, J. Phys. Chem. Solids 30, 643 (1969).
¹⁹M. O. Vassell, J. Math. Phys. 11, 408 (1970).
²⁰A. D. Boardman, W. Fawcett, and H. D. Rees, Solid State Commun. 6, 305 (1968).
²¹H. Ehrenreich, J. Phys. Chem. Solids 8, 130 (1959).
²²J. D. Zook, Phys. Rev. 136, A869 (1964).
²³A. R. Hutson, J. Appl. Phys. 32, 2287 (1961).
²⁴F. Seitz, *Modern Theory of Solids* (McGraw-Hill, New York, 1940), p. 376ff.
²⁵D. G. Seiler, Phys. Letters 31A, 309 (1970).
²⁶O. Madelung, *Physics of III-V Compounds* (Wiley, New York, 1964).
²⁷M. Cardona, in *Semiconductors and Semimetals*, edited by R. K. Willardson and A. C. Beer (Academic, New York, 1966), Vol. 3, p. 151.
²⁸B. O. Seraphin and H. E. Bennett, in Ref. 27.
²⁹M. Hass, in Ref. 27, p. 11.
³⁰G. Arlt and P. Quadflieg, Phys. Status Solidi 25, 323 (1968).
³¹J. C. Phillips and J. A. Van Vechten, Phys. Rev. Letters 23, 1115 (1969).
³²G. Busch and E. Steigmeier, Helv. Phys. Acta 34, 1 (1961).
³³H. J. Hrostowski, F. J. Morin, T. H. Geballe, and G. H. Wheatley, Phys. Rev. 100, 1672 (1955).
³⁴R. W. Cunningham and J. B. Gruber, J. Appl. Phys. 41, 1804 (1970).
³⁵N. I. Volokobinskaya, V. V. Galavanov, and D. N. Nasledov, Fiz. Tverd. Tela 1, 756 (1959) [Sov. Phys. Solid State 1, 687 (1959)].
³⁶J. C. McGroddy, M. R. Lorenz, and T. S. Plaskett, Solid State Commun. 7, 901 (1969); J. E. Smith, Jr. (private communication).
³⁷See Ref. 26, p. 118.
³⁸C. Hilsum and A. C. Rose-Innes, *Semiconducting III-V Compounds* (Pergamon, New York, 1961), p. 128.
³⁹A. S. Filipchenko and D. N. Nasledov, Phys. Status Solidi 19, 435 (1967).
⁴⁰R. Barrie and J. T. Edmond, J. Electron. 1, 161 (1955).
⁴¹A. I. Blum and G. P. Ryabtsova, Fiz. Tverd. Tela 1, 761 (1959) [Sov. Phys. Solid State 1, 692 (1959)].
⁴²H. Weiss, Z. Naturforsch. 11a, 131 (1956).
⁴³C. J. Summers and S. D. Smith, Proc. Phys. Soc. (London) 92, 215 (1967).
⁴⁴O. G. Lorimer and W. G. Spitzer, J. Appl. Phys. 36, 1841 (1965).
⁴⁵See Ref. 38, p. 181.
⁴⁶T. S. Moss, *Optical Properties of Semiconductors* (Academic, New York, 1959), p. 224.
⁴⁷T. C. Harman, H. L. Goering, and A. C. Beer, Phys. Rev. 104, 1562 (1956).
⁴⁸O. G. Folberth, O. Madelung, and H. Weiss, Z. Naturforsch. 9a, 954 (1954).
⁴⁹J. P. McCarthy, Solid State Electron. 10, 649 (1967).
⁵⁰N. Godinho and A. Brunnschweiler, Solid State Electron. 13, 47 (1970).
⁵¹G. R. Cronin and S. R. Borello, J. Electrochem. Soc. 114, 1078 (1967).
⁵²W. Fawcett, C. Hilsum, and H. D. Rees, Solid State Commun. 7, 1257 (1969).
⁵³See Ref. 38, p. 132.
⁵⁴F. J. Reid, in *Compound Semiconductors*, edited by R. K. Willardson and H. L. Goering (Reinhold, New York, 1962), Vol. 1, p. 158.
⁵⁵G. R. Cronin, R. W. Conrad, and S. R. Borello, J. Electrochem. Soc. 113, 1336 (1966).
⁵⁶V. A. Vlasov and S. A. Semiletov, Kristallografiya 13, 683 (1968) [Sov. Phys. Crist. 13, 580 (1969)].
⁵⁷J. P. McCarthy, Solid State Commun. 5, 5 (1967).
⁵⁸Data compiled and expanded by F. P. Kesamanly, Yu. V. Mal'tsev, D. N. Nasledov, L. A. Nikolaeva, M. N. Pivovarov, V. A. Skripkin, and Yu. I. Ukanov, Sov. Phys. Semiconductors 3, 993 (1970).
⁵⁹M. Cardona, K. L. Shaklee, and F. H. Pollak, Phys. Rev. 154, 696 (1967).
⁶⁰M. Cardona, J. Phys. Chem. Solids 24, 1543 (1963).
⁶¹M. Balkanski and E. Amzallag, Phys. Status Solidi 30, 407 (1968).
⁶²P. Lawaetz, by a five-level $\bar{k} \cdot \bar{p}$ analysis, also finds

m^* in InP to be larger than that in GaAs, the ratio being 1.04 compared to our ratio (see Ref. 4) of 1.09 (private communication).

⁶³C. Hilsun, S. Fray, and C. Smith, *Solid State Commun.* **7**, 1057 (1969).

⁶⁴L. Kleinman, *Phys. Rev.* **128**, 2614 (1962).

⁶⁵O. G. Folberth and H. Weiss, *Z. Naturforsch.* **10a**, 615 (1955).

⁶⁶V. V. Galavanov and N. V. Siukaev, *Phys. Status Solidi* **38**, 523 (1970).

⁶⁷L. W. James, J. P. VanDyke, F. Herman, and D. M. Chang, *Phys. Rev. B* **1**, 3998 (1970).

⁶⁸F. J. Reid and R. K. Willardson, *J. Electron.* **5**, 54 (1958).

⁶⁹M. Glicksman and K. Weiser, *J. Electrochem. Soc.* **105**, 728 (1958).

⁷⁰T. C. Harman, J. I. Genco, W. P. Allred, and H. L. Goering, *J. Electrochem. Soc.* **105**, 731 (1958).

⁷¹F. P. Kesamanly, D. N. Nasledov, A. Ya. Nashel'skii, and V. A. Skripkin, *Fiz. Zekh. Poluprov.* **2**, 1463 (1968) [*Sov. Phys. Semicond.* **2**, 1221 (1969)] (1969)].

⁷²O. Roder, thesis (Goethe University, Frankfurt, 1969) (unpublished); O. Roder, U. Heim, and M. H. Pilkuhn, *J. Phys. Chem. Solids* (to be published).

⁷³M. Glicksman, *J. Phys. Chem. Solids* **8**, 511 (1959).

⁷⁴I. Kudman and E. F. Steigmeier, *Phys. Rev.* **133**, A1665 (1964).

⁷⁵G. G. Kovalevskaya and S. V. Slobodchikov, *Phys. Status Solidi* **30**, 441 (1968).

⁷⁶D. Richman, in Ref. 54, p. 214.

⁷⁷R. C. Clarke, B. D. Joyce, and W. H. E. Wilgoss, *Solid State Commun.* **8**, 1125 (1970).

⁷⁸Earlier data from various sources compiled in Ref. 71.

Coulomb Effects at Saddle-Type Critical Points in CdTe, ZnTe, ZnSe, and HgTe

Y. Pétroff and M. Balkanski

*Laboratoire de Physique des Solides de la Faculté des Sciences de Paris
Equipe de Recherche, associée au Centre National de la Recherche Scientifique
Paris, France*

(Received 13 October 1970)

The Kane model for saddle-point excitons is applied to CdTe, ZnTe, ZnSe, and HgTe by studying the shape of the imaginary part of the dielectric constant ϵ_2 obtained by reflectivity measurements at 10°K. We have obtained $|m_3/m_1| = 28$ for CdTe and 20 for ZnTe but we have not been able to measure the ratio for ZnSe or HgTe.

The effect of the interaction between electron and hole at an M_1 critical point is a very controversial problem.¹ An experimental approach² to this problem was suggested several years ago by Cardona and Harbeke. In the last few years, several theoreticians³⁻⁵ have treated the subject, but the first complete calculation was only performed quite recently by Kane.¹ He based his calculation on the fact that, at the L point, in the blende structure, $m_1 = m_2 > 0$ and $|m_3| \gg m_1$, where m_1 , m_2 , and m_3 are the principal effective masses. Kane used the adiabatic approximation to solve the Schrödinger equation of the exciton:

$$\left(\frac{p_1^2}{2m_1} + \frac{p_2^2}{2m_2} + \frac{p_3^2}{2m_3} - \frac{e^2}{Kr} \right) \Phi(r) = E\Phi(r), \quad (1)$$

where $\Phi(r)$ is the envelope function.

The imaginary part of dielectric constant ϵ_2 is written

$$\epsilon_2 = \frac{4\pi^2 e^2}{3m^2 \omega^2 V} \sum_f |P_{if}|^2 \delta(E_f - E_i - \hbar\omega), \quad (2)$$

where

$$P_{if} = \langle U_i | P | U_f \rangle \Phi(0) \sqrt{V}$$

is the matrix element of momentum between initial

and final states, U_i and U_f are the cell periodic parts of the Bloch function at critical point, and V is the volume.

Following Kane's calculation, Eq. (2) can be written

$$\epsilon_2(\omega) = 8\pi^2 \frac{(m_{r\perp}/m_0)^2 \langle P^2 \rangle_{av}}{3m_0^2 a_0^2 K_\infty} N \frac{S_{tot}}{\omega^2}, \quad (3)$$

where a_0 is Bohr radius, $N=4$ is number of critical points, $\langle P^2 \rangle_{av} = 3 \langle P_x^2 \rangle_{av} = P^2$, K_∞ is the dielectric constant, $m_{r\perp}$ is the reduced mass, and $S_{tot}(\omega)$ is a function taking into account the continuum structure and the structure associated with the two-dimensional bound state. The peak is asymmetric and drops sharply on the high-energy side.

In Fig. 1 we have plotted the reflectivity curves⁶ of CdTe, ZnTe, ZnSe, and HgTe, in the region of

Λ_{4v} , $\Lambda_{5v} \rightarrow \Lambda_{6c}$ transition,

$\Lambda_{6v} \rightarrow \Lambda_{6c}$ transition.

These curves were obtained with the sample temperature at 10°K by an apparatus described previously.⁷ The excitonic peaks and the structure of the critical point are clearly seen for CdTe and ZnTe. However, we do not observe the critical-point